

# 1        **Backstress from dislocation interactions quantified** 2        **by nanoindentation load-drop experiments**

3        Christopher A. Thom<sup>1</sup>, Lars N. Hansen<sup>2</sup>, David L. Goldsby<sup>3</sup>, & Kathryn M. Kumamoto<sup>1,2</sup>

4        <sup>1</sup>Department of Earth Sciences, University of Oxford, Oxford, OX1 3AN, U.K.

5        <sup>2</sup>Department of Earth and Environmental Sciences, University of Minnesota-Twin Cities, Minneapolis,  
6        Minnesota, 55455, U.S.A.

7        <sup>3</sup>Department of Earth and Environmental Science, University of Pennsylvania, Philadelphia, Pennsylvania,  
8        19104, U.S.A.

## 9        **Key Points**

- 11        • A nanoindentation load drop method was used to measure backstress in a material with a high  
12        dislocation density at sub-micron length scales.
- 13        • The backstresses measured in three geologic materials agree with theoretical predictions of Taylor  
14        hardening.
- 15        • Backstresses result from long-range dislocation interactions, an athermal process that can occur  
16        over a range of deformation conditions.

## 17        **Abstract**

18        Recent work has identified the importance of strain hardening and backstresses among dislocations  
19        in the deformation of geologic materials at both high and low temperatures, but very few experimental  
20        measurements of such backstresses exist. Using a nanoindentation load drop method and a self-similar  
21        Berkovich tip, we measure backstresses in single crystals of olivine, quartz, and plagioclase feldspar at a  
22        range of indentation depths from 100–1750 nm, corresponding to densities of geometrically necessary  
23        dislocations (GND) of order  $10^{14}$ – $10^{15}$  m<sup>-2</sup>. Our results reveal a power-law relationship between backstress

24 and GND density, with an exponent ranging from 0.44 to 0.55 for each material, in close agreement with  
25 the theoretical prediction (0.5) from Taylor hardening. This work provides experimental evidence of Taylor  
26 hardening in geologic materials and supports the assertion that backstress must be considered in both high-  
27 and low-temperature deformation.

## 28 **Plain Language Summary**

29 As a material is plastically deformed at room temperature, it often becomes stronger. In minerals,  
30 this strengthening is typically caused by the accumulation of linear defects within the material. These  
31 defects repel each other and push back with a strength predicted to be proportional to the square root of the  
32 defect density, but this relationship has not typically been observed for geologic materials. We developed  
33 a method to measure the strength of this pushback at very small scales for which the density of these defects  
34 in the crystal is high. Our results for three common geologic materials agree with predictions from theory  
35 and demonstrate that these defects must be considered when modeling deformation of rocks in Earth's  
36 interior.

## 37 **1. Introduction**

38 The transient rheology of the upper mantle is inferred to control the dynamics of many geologic  
39 phenomena, including post-seismic deformation (e.g., Freed et al., 2012; Wang et al., 2012; Hu et al., 2016;  
40 Qiu et al., 2018). Several studies have presented models to describe the transient rheological behavior  
41 following large earthquakes (e.g., Masuti et al., 2016; Moore et al., 2017; Muto et al., 2019), but the physical  
42 mechanism that gives rise to this complex time-dependent rheology is not well-constrained. For example,  
43 Masuti et al. (2016) used a strain hardening coefficient to modify a stress element in their Burgers model,  
44 but noted that the functional form of the constitutive law was completely unknown.

45 Experiments on geologic materials have measured transient creep (e.g., Post, 1977; Durham et al.,  
46 1979; Gangi, 1983; Duval et al., 1983; Smith & Carpenter, 1987; Hanson & Spetzler, 1994; Chopra, 1997;  
47 Caswell et al., 2015; Hansen et al., 2020), but quantifying this rheological behavior using conventional  
48 creep experiments is challenging because it may be caused by the interplay of multiple deformation

49 processes acting simultaneously. Examination of the microstructures in recent stress-reduction experiments  
50 on olivine single crystals by Hansen et al. (2020) suggested that time-dependent recoverable strain (i.e.,  
51 anelasticity) at high temperatures arises due to a combination of high-temperature deformation mechanisms,  
52 dislocation glide, and long-range elastic interactions among dislocations. These authors presented a  
53 microphysical model that arises naturally from the behavior of lattice dislocations and captures both  
54 transient and steady-state rheology over a wide range of conditions. Specifically, Hansen et al. (2020)  
55 suggested that geometrically necessary dislocations (GNDs), which are dislocations of the same sign  
56 needed to accommodate lattice curvature or gradients in local strain, are an important defect type controlling  
57 transient deformation at high temperature. These dislocations differ from statistically stored dislocations  
58 (SSDs) in that the lattice distortion of GNDs is not cancelled by dislocations of the opposite sign.  
59 Consequently, GNDs can exhibit long-range interactions over length scales of 1–100 microns (Wallis et  
60 al., 2017; 2020a; 2020b). These interactions ultimately lead to a backstress which opposes further  
61 deformation by dislocation glide.

62         Recent work also identified backstresses at much higher total GND densities in olivine deformed  
63 by low-temperature plasticity (Hansen et al., 2019; Wallis et al., 2020a). In addition to identifying a length  
64 scale effect in the yield stress (effectively the Hall-Petch effect), Hansen et al. (2019) also demonstrated the  
65 presence of strain hardening and the Bauschinger effect, a well-known phenomenon in metallurgical  
66 literature wherein the yield stress of a material is reduced after the deformation direction is reversed (i.e.,  
67 the yield stress in extension is reduced after initially yielding in compression, and vice versa). This  
68 phenomenon is commonly attributed to the effect of an internal backstress from GND interactions that acts  
69 in the opposite direction to the initial deformation (Dieter, 1986 Chapters 4.14, 6.16, and references therein).  
70 Using high-angular resolution electron backscatter diffraction (HR-EBSD), Wallis et al. (2020a) measured  
71 the GND density of a deformed single crystal of olivine from Hansen et al. (2019) and demonstrated that  
72 the Bauschinger effect was indeed related to long-range elastic interactions among GNDs created during  
73 strain hardening. Wallis et al. (2020a) also identified similar microstructures beneath indents in olivine  
74 from Kumamoto et al. (2017), suggesting that the same physical mechanism (i.e., hardening due to

75 dislocation interactions) occurs during nanoindentation. However, due to the significantly larger stresses in  
76 nanoindentation, the dislocation density was much higher than in samples deformed in Hansen et al. (2019).

77 In the present paper, we quantify the relationship between GND density and backstress in three  
78 common geologic materials (olivine, quartz, and plagioclase feldspar) using a novel nanoindentation  
79 method. Because nanoindentation localizes deformation in a small volume of material, the sample is  
80 essentially self-confined, and extremely high stresses can be applied without inducing fracture.  
81 Additionally, nanoindentation using a Berkovich (3-sided pyramid) tip offers a significant advantage in that  
82 it can be used to probe different microstructures (i.e., GND densities) at the same strain (~8%) due to its  
83 self-similar geometry. We utilize this technique to demonstrate excellent quantitative agreement between  
84 our experiments and theoretical predictions of Taylor hardening (Taylor, 1934), which suggests that  
85 backstress should scale as the square root of GND density.

## 86 **2. Methods**

87 We have developed a method to measure the backstress from GNDs created during nanoindentation  
88 experiments. This method is similar to a stress-reduction test, a common technique used on macroscopic  
89 samples to measure anelasticity (e.g., Takeuchi & Argon, 1976; Blum & Weckert, 1987; Caswell et al.,  
90 2015; Hansen et al., 2020), with one key difference. Because the indentation stress is controlled by the  
91 mechanical response of the sample and not its physical dimensions, this type of experiment is more  
92 accurately described as a “load-drop” test. Only the applied load is prescribed in the experiment, and neither  
93 stress nor strain rate are controlled. Syed Asif and Pethica (1997) presented the only previous study that  
94 utilized load drops to measure changes in indentation creep behavior, but they did not quantify the  
95 backstress systematically in their study of tungsten and gallium arsenide single crystals.

96 Each of our experiments consisted of four parts: 1) an initial loading phase, 2) a short hold at  
97 constant load to measure indentation creep behavior, 3) a rapid load drop, and 4) another longer hold at a  
98 reduced constant load to measure the mechanical response of the sample. Segment 1 can be completed  
99 using any number of standard nanoindentation protocols, such as constant loading rate or constant nominal

100 strain rate, as the main function of this step is to set the initial microstructure (i.e., GND density) beneath  
101 the indenter tip. The GND density,  $\rho_{\text{GND}}$ , below the indenter tip for a pyramidal geometry is a function of  
102 the tip shape, the indentation depth,  $h$ , and the Burgers vector,  $b$ , of the material (e.g. Pharr et al., 2010) and  
103 is given by

$$\rho_{\text{GND}} = \frac{3 \tan^2 \theta}{2bh}, \quad (\text{Eq. 1})$$

104 where  $\theta$  is the angle formed between the surface and the indenter ( $19.7^\circ$  for a Berkovich tip). Thus, deeper  
105 indents formed by larger applied loads will result in a lower GND density.  
106

107 In the results presented here, all experiments were performed in a load-controlled nanoindentation  
108 apparatus with  $\dot{P}/P = 0.2$  for segment 1, where  $P$  is the applied load and  $\dot{P}$  is its time derivative. The  
109 indentation hardness,  $H$ , is the mean contact stress, defined as

$$H = \frac{P}{A}, \quad (\text{Eq. 2})$$

110 where  $A$  is the projected contact area between the tip and the sample. The value of  $A$  is calibrated as a  
111 function of depth using a standard of known Young's modulus (usually fused silica) and given by the  
112 relationship  
113

$$A = C_1 h_c^2 + C_2 h_c + C_3 h_c^{\frac{1}{2}} + \dots + C_7 h_c^{\frac{1}{32}}, \quad (\text{Eq. 3})$$

114 where  $C_1, C_2, C_3 \dots C_7$  are constants, and  $h_c$  is the contact depth (i.e., the true depth at which the tip and  
115 sample are in contact, with elastic deflection of the surface of the sample removed). The contact depth is  
116 given by  
117

$$h_c = h - \epsilon \frac{P}{S}, \quad (\text{Eq. 4})$$

118 where  $h$  is the measured indentation depth,  $\epsilon$  is a constant associated with the geometry of the indenter ( $0.75$   
119 for Berkovich), and  $S$  is the contact stiffness. With known contact stiffness and contact area, the reduced  
120 elastic modulus,  $E_r$ , of the tip-sample contact can be determined using  
121

$$E_r = \frac{\sqrt{\pi} S}{2\sqrt{A}}. \quad (\text{Eq. 5})$$

122

123 Utilizing known values of the elastic constants of the diamond tip and an assumed Poisson's ratio of the  
124 sample, we determined the sample's elastic modulus using

$$125 \quad \frac{1}{E_r} = \frac{1 - \nu_s^2}{E_s} + \frac{1 - \nu_i^2}{E_i}, \quad (\text{Eq. 6})$$

126 where  $E$  is the Young's modulus,  $\nu$  is Poisson's ratio, and the subscripts  $s$  and  $i$  refer to the sample and  
127 indenter tip, respectively. Our experiments were performed using the continuous stiffness measurement  
128 (CSM) method with a dynamic frequency of 110 Hz and a target dynamic displacement of 2 nm, which  
129 allowed us to measure the contact stiffness (and therefore the contact depth, hardness, and elastic modulus  
130 of the sample) continuously as a function of time (Li & Bhushan, 2002; Oliver & Pharr, 2004).

131 Segment 2 of our load-drop method is optional, but in these experiments we performed a 60-s hold  
132 to measure the creep behavior. Due to possible thermal drift of the instrument, this portion of the test and  
133 all subsequent measurements were obtained using the CSM method. In this portion of the test, and all  
134 following steps, we used the measured elastic modulus from Segment 1 and rearrange Eq. 5 to solve for  
135 contact area as

$$136 \quad A = \frac{\pi S^2}{4E_r^2}. \quad (\text{Eq. 7})$$

137 This approach is preferable to relying on the depth measurement to acquire contact area using Eqs. 3 and 4  
138 because the depth measurement is highly sensitive to temperature fluctuations. Thus, our subsequent  
139 measurements of hardness from Eq. 2 are calculated from the measured contact stiffness, the previously  
140 derived elastic modulus, and the current applied load.

141 Segments 3 and 4 are the additions of our method and encompass a load drop and subsequent hold.  
142 In Segment 3 of our experiments, we reduced the load linearly over 1 s by a prescribed amount, ranging  
143 from 1% to 99% of the maximum applied load. A small amount of dynamic overshoot occurred for large  
144 reductions in applied load, but these variations did not significantly influence any of our results. After the  
145 load drop, the new applied load was held constant for the duration of Segment 4. In the results presented  
146 here, we held the load at the reduced value for 3600 s before completely unloading the sample.

147           In summary, this method determines the hardness and elastic modulus as a function of indentation  
148 depth and the creep behavior during a short hold at high stress. In addition, by testing a range of reductions  
149 in load for a given peak load, we can determine the magnitude of the backstress in a material, as  
150 demonstrated below. Repeating a series of experiments at different peak loads and thus different maximum  
151 depths, corresponding to different GND densities, also allows us to explore the influence of microstructure  
152 on backstress.

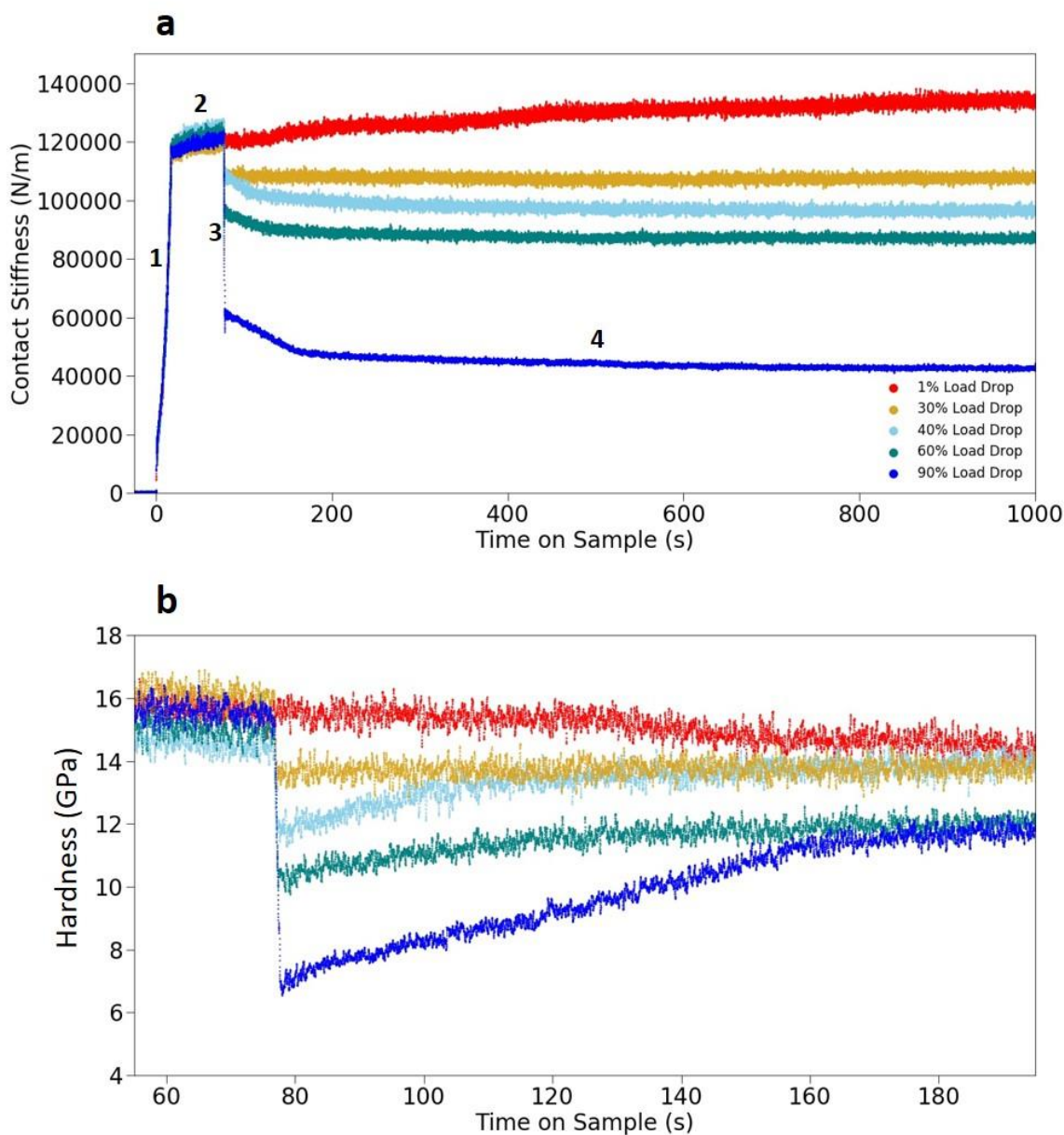
### 153 **3. Results**

154           We performed a total of 155 load-drop experiments on single crystals of San Carlos olivine,  
155 synthetic quartz, and natural plagioclase feldspar (labradorite). For each experiment, we recorded the  
156 applied load, indentation depth, and contact stiffness at a rate of 100 Hz, from which we derived the elastic  
157 modulus, hardness, and creep behavior at each point in the test.

158           For each material, Segments 1 and 2 were reproducible for a given maximum load (e.g., Figure 1a),  
159 and the values obtained for the elastic modulus and scale-dependent hardness were consistent with previous  
160 results on the same materials (Kumamoto et al., 2017; Thom et al., 2018). To discuss the results from  
161 Segments 3 and 4, we examine a representative set of experiments on olivine presented in Figure 1. In each  
162 experiment, the maximum applied load was 5 mN; thus the indentation depth (120 nm) and GND density  
163 ( $29.6 \times 10^{14} \text{ m}^{-2}$ ) (Table 1) immediately prior to the load drops were approximately equivalent (Eq. 1). The  
164 only difference among these experiments was the magnitude of the load drop during Segment 3 of each  
165 test. Contact stiffness versus time for each experiment before and after the load drop are presented in Figure  
166 1a, with each test segment labeled. An initial steep increase in contact stiffness occurs in Segment 1, and a  
167 small increase over time occurs in Segment 2. The abrupt reduction in contact stiffness occurs as the applied  
168 stress is reduced in Segment 3 and is associated with some elastic recovery of the material.

169           In all experiments, one of three behaviors was observed after the load drop: 1) the contact stiffness  
170 increased with time (forward creep), 2) the contact stiffness decreased with time (backwards/reverse creep),  
171 or 3) there was no change in contact stiffness (negligible/no creep). In the examples in Figure 1a, one test

172 demonstrates continued forward creep (1% load drop), three tests demonstrate backwards creep in the early  
173 portions of the hold (40%, 60%, and 90% load drops), and one test exhibits no change in the stiffness (30%  
174 load drop). The transition from backwards creep to no creep is taken to be the point at which the applied  
175 stress is approximately equal to the backstress from dislocation interactions.



176  
177 *Figure 1: Contact stiffness (a) and hardness (b) vs. time on sample for five experiments on olivine at a peak*  
178 *load of 5 mN. The steep rise in stiffness at the beginning of the test in (a) represents Segment 1 of the*  
179 *experiment and the slow increase in stiffness over time in Segment 2 is due to creep (both labeled). Upon*



180 unloading by different percentages of the same peak load (Segment 3), both contact stiffness (a) and  
181 hardness (b) decrease due to some elastic recovery of the samples. During Segment 4, contact stiffness  
182 either continues to increase over time due to forward creep (e.g., for a 1% load drop), decreases due to  
183 reverse creep (e.g., for a 90% load drop), or remains constant over time (i.e., no creep as shown by the  
184 30% load drop). The corresponding response in hardness is shown in (b), where the hardness decreases  
185 (forward creep), increases (backwards creep), or remains the same (no creep).

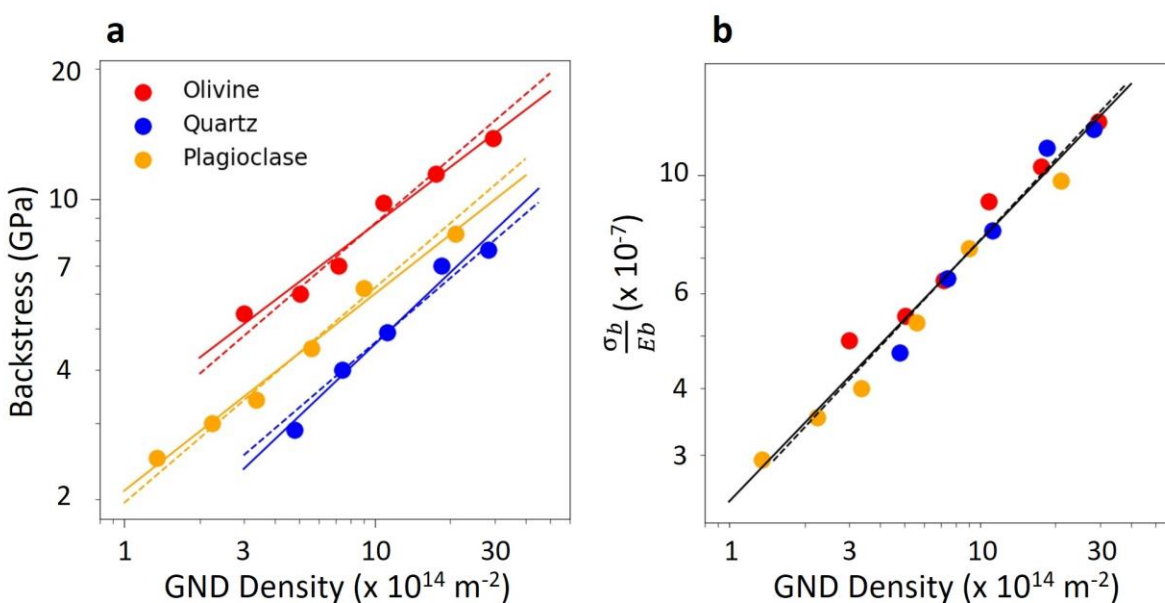
186 We use the measured contact stiffness, the elastic modulus calculated from Segment 1, and Eqs. 2  
187 and 7 to determine the hardness in the experiments in Figure 1a. These data are presented in Figure 1b for  
188 a portion of the experiments shortly before and after the load drop. For a load drop of 1%, hardness  
189 decreases slightly over time due to forward creep, consistent with previous nanoindentation creep  
190 experiments (e.g., Thom & Goldsby, 2019). Tests in which the backstress exceeds the applied stress result  
191 in an increase in the measured hardness over time after the load drop (40%, 60%, and 90% load drops), and  
192 the experiment with no creep (30% load drop) shows constant hardness with time. The hardness for the  
193 experiment with the 30% load drop in Figure 1b is 13.8 GPa, which we infer to be the backstress associated  
194 with the GND density in these experiments.

195 By varying the maximum applied load and thereby reaching different initial indentation depths, we  
196 are able to probe the backstress of each material over GND densities varying by approximately one order  
197 of magnitude. A summary of the data used to construct Figure 2a is presented in Table 1. Each data point  
198 is derived from a series of experiments like those in Figure 1. For each material, a best-fit line is marked  
199 by the solid line of the respective color, with power-law exponents of 0.44, 0.55, and 0.46 for olivine,  
200 quartz, and feldspar, respectively. The average exponent across the materials is 0.49. In addition, a dashed  
201 line of the same color is forced through the data with a slope of 0.5, representing the theoretical fit from the  
202 hardening component of the Taylor equation (Taylor, 1934), which is given by

$$203 \quad \sigma_b = \alpha G b \sqrt{\rho_{\text{GND}}}, \quad (\text{Eq. 8})$$

204 where  $\sigma_b$  is the backstress associated with hardening from GNDs,  $\alpha$  is a constant,  $G$  is the shear modulus,  
205 and  $b$  is the Burgers vector. For each material, the data are adequately fit by the dashed lines, but because

206 the data only span one order of magnitude in GND density, it is difficult to evaluate the robustness of the  
 207 fits, similar to previous assessments of the Hall-Petch effect (Dunstan & Bushby, 2014; Li et al., 2016).  
 208 Normalizing the backstress by the Young's modulus derived from the indentation tests and the Burgers  
 209 vector of the material reveals remarkable data collapse, as shown in Figure 2b. A solid black line represents  
 210 the best fit to all normalized data with a slope of 0.49, and a dashed black line is presented with a slope of  
 211 0.5 for comparison to the theoretical prediction. This agreement suggests that the value of  $\alpha$  in the Taylor  
 212 equation is the same for all materials tested here (approximately 3.7).



213  
 214 *Figure 2: Results of all experiments on olivine, quartz, and plagioclase feldspar demonstrating that*  
 215 *backstress (a) and normalized backstress (b) are a function of the initial microstructure, or GND density.*  
 216 *Each data point in (a) and (b) is found using a series of experiments like those depicted in Figure 1. The*  
 217 *solid lines in (a) are best fits to each individual set of data (slope of 0.44 for olivine, 0.55 for quartz, and*  
 218 *0.46 for plagioclase feldspar, with an average value of 0.49), and each dotted line is the forced fit of a line*  
 219 *with a slope of 0.5, which is predicted from the Taylor hardening equation. In (b), the backstress is*  
 220 *normalized by the Young's modulus derived from Segment 1 of the indentation test (200 GPa for olivine,*  
 221 *120 GPa for quartz, and 105 GPa for plagioclase feldspar) and the appropriate Burgers vector (0.55, 0.52,*

222 and 0.81 nm, respectively). The solid black line is a best fit to all the normalized data with a slope of 0.49,

223 and the dashed black line is a forced fit to the data with a slope of 0.5.

224

225 *Table 1: Target maximum applied load, average maximum indentation depth, backstress, and GND density*  
 226 *for all data presented in Figure 2a.*

Sample	Maximum Load (mN)	Indentation Depth (nm)	Backstress (GPa)	GND Density ( $\times 10^{14} \text{ m}^{-2}$ )
Olivine	5	120	13.8	29.6
	15	200	11.4	17.6
	25	320	9.8	10.8
	65	480	7.0	7.2
	100	690	6.0	5.0
	300	1150	5.4	3.0
Quartz	5	130	7.6	28.4
	10	200	7.0	18.5
	25	330	4.9	11.2
	50	500	4.0	7.4
	100	780	2.9	4.8
Plag	2	110	8.3	21.1
	10	260	6.2	9.1
	25	420	4.5	5.6
	70	700	3.4	3.4
	150	1050	3.0	2.2
	400	1750	2.5	1.4

227

228

229

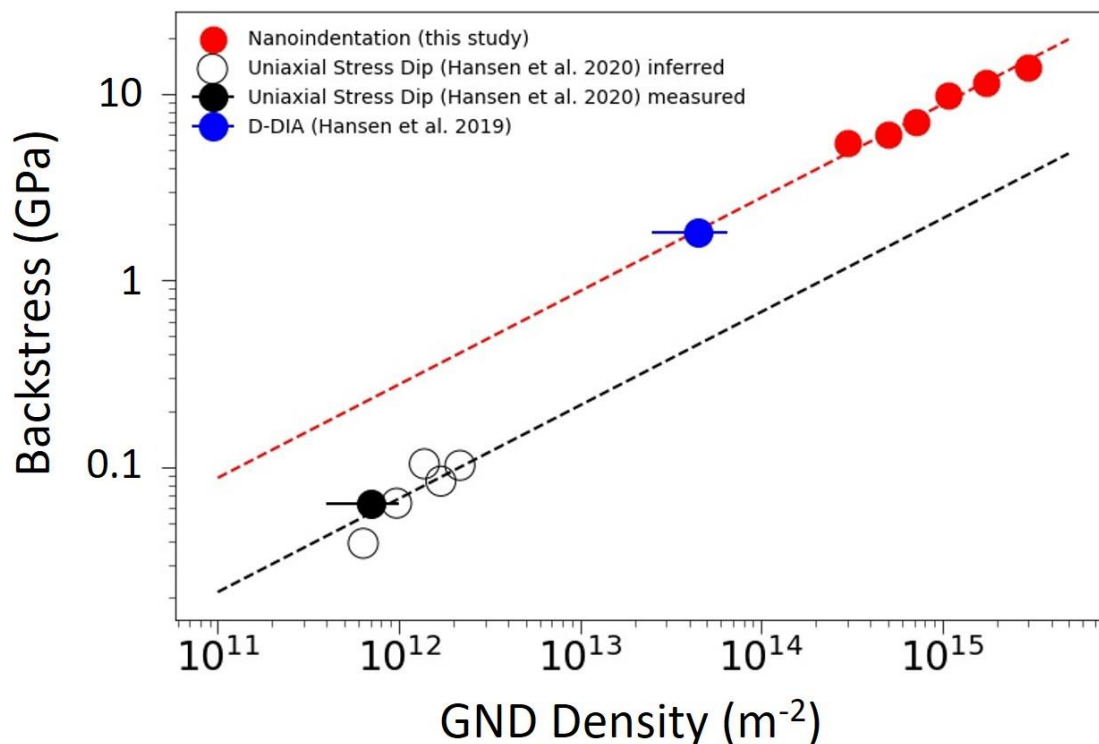
230

231

## 232 **4. Discussion**

233 We compare our olivine data to other measurements of backstress and GND density in single  
234 crystals of olivine in Figure 3. Data from this study are shown in red at high GND density, data from a  
235 room-temperature deformation-DIA (D-DIA) experiment of Hansen et al. (2019) are shown in blue at  
236 intermediate GND density, and data from the high-temperature (1573 K) experiments of Hansen et al.  
237 (2020) are shown in black at the lowest GND density. The solid black data point represents a sample where  
238 the GND density was directly measured, and the open black circles represent GND densities inferred by  
239 using the dislocation density piezometer of Bai & Kohlstedt (1991) and assuming all dislocations are GNDs.  
240 We note that the inferred GND density of the sample with a direct measurement is within the error bars,  
241 suggesting our assumption of all dislocations being GNDs is reasonable. The dashed red line presented in  
242 Figure 3 is the same as in Figure 2a (it is only fit to the nanoindentation data), while the black dashed line  
243 is a forced fit of the Taylor equation to the high-temperature data. The room-temperature experiment of  
244 Hansen et al. (2019) falls on the same line as the indentation data presented here, while the high-temperature  
245 data appear to be systematically offset to lower backstresses (i.e., with a smaller value of  $\alpha$ ).

246 While we do not observe a universal relationship between high- and low-temperature experiments,  
247 these results are consistent with the microphysical model presented by Hansen et al. (2020), in which  
248 transient and steady-state rheology are captured by a combination of dislocation glide, elastic interactions  
249 among GNDs, and recovery mechanisms. The value of  $\alpha$  may be temperature-dependent or a function of  
250 the differential stress, but more experiments at intermediate conditions are needed to resolve this subtlety.  
251 However, this study provides direct evidence of Taylor hardening in geologic materials at room  
252 temperature, and future work will explicitly link the Taylor equation (i.e., the evolution of backstress with  
253 GND density) to transient rheology over a wide range of conditions. The presence of Taylor hardening in  
254 all minerals tested here and the remarkable data collapse presented in Fig. 2b suggests that transient  
255 deformation of other geologic materials may be parameterized in a similar manner to that in Hansen et al.  
256 (2019; 2020), and that microstructural evolution models must incorporate the Taylor relationship.



257  
 258 *Figure 3: Compilation of backstress and GND density data from studies of single crystals of San Carlos*  
 259 *olivine which measure both values. Results from room temperature indentation tests (this study) are shown*  
 260 *in red, the room temperature D-DIA experiment from Hansen et al. (2019) analyzed by Wallis et al. (2020a)*  
 261 *is shown in blue, and the high temperature stress dip experiments from Hansen et al. (2020) are shown in*  
 262 *black (the direct GND measurement is represented by the solid circle, while inferred GND values are*  
 263 *represented by the open circles). Horizontal error bars reflect uncertainty in the average GND density*  
 264 *determined via HR-EBSD. The dashed red and black lines are fits of the Taylor hardening equation for the*  
 265 *nanoindentation and high-temperature stress dips, respectively.*

## 266 5. Conclusions

267 We have performed nanoindentation load-drop experiments on single crystals of olivine, quartz,  
 268 and plagioclase feldspar to measure the backstress created by long-range elastic interactions among  
 269 dislocations. To vary the GND density, we applied a range of maximum loads using a self-similar

270 Berkovich indenter tip to achieve a range of indentation depths. Our results demonstrate that the  
271 backstress in all three materials scales approximately with the square root of GND density, as predicted  
272 from the Taylor hardening equation. The value of  $\alpha$  in the Taylor equation is similar among all materials  
273 tested here at room temperature but varies from that inferred in high-temperature experiments, suggesting  
274 that recovery or stress may play a role in modifying the backstress. However, these results are consistent  
275 with the microphysical model presented by Hansen et al. (2020), which suggests that backstress and its  
276 evolution are important physical processes that must be considered in studies of deforming geologic  
277 materials, including during transient deformation at both high- and low-temperature.

## 278 **Acknowledgements**

279 C.A.T. designed the study and nanoindentation method, carried out experiments and data  
280 analysis, and wrote the initial manuscript draft. All authors contributed to editing and revising the  
281 manuscript. The authors would like to thank G. Pharr, T. Breithaupt, and D. Wallis for useful discussions.  
282 All data used in this study are available at <https://upenn.box.com/s/mo9txpz9n6dzvdup6dt5yq8t6ltd80tt>.  
283 Funding for this study was provided by NERC 1710DG008/JC4 to L.N.H. and C.A.T. and NSF EAR-  
284 1806791 to K.M.K.

## 285 **References**

- 286 1. Bai, Q., Mackewll, S.J., & Kohlstedt, D.L. (1991). High-temperature creep of olivine single crystals  
287 1. Mechanical results for buffered samples. *Journal of Geophysical Research*, 96(B2), 2241-2463.  
288 <https://doi.org/10.1029/90JB01723>
- 289 2. Blum, W., & Weckert, E. (1987). On the interpretation of the “internal stress” determined from dip  
290 tests during creep of Al-5at.%Mg. *Materials Science and Engineering*, 86, 145-158.  
291 [https://doi.org/10.1016/0025-5416\(87\)90449-6](https://doi.org/10.1016/0025-5416(87)90449-6)
- 292 3. Caswell, T.E., Cooper, R.F., & Goldsby, D.L. (2015). The constant-hardness creep compliance of  
293 polycrystalline ice. *Geophysical Research Letters*, 42(15), 6261-6268.  
294 <https://doi.org/10.1002/2015GL064666>

- 295 4. Chopra, P.N. (1997). High-temperature transient creep in olivine rocks. *Tectonophysics*, 279(1-4),  
296 93-111. [https://doi.org/10.1016/S0040-1951\(97\)00134-0](https://doi.org/10.1016/S0040-1951(97)00134-0)
- 297 5. Dieter, G.E. (1986). *Mechanical Metallurgy*. New York, NY: McGraw-Hill Education.
- 298 6. Dunstan, D.J., & Bushby, A.J. (2014). Grain size dependence of the strength of metals: The Hall–  
299 Petch effect does not scale as the inverse square root of grain size. *International Journal of*  
300 *Plasticity*, 53, 56-65. <https://doi.org/10.1016/j.ijplas.2013.07.004>
- 301 7. Durham, W.B., Froidevaux, C., & Jaoul, O. (1979). Transient and steady-state creep of pure  
302 forsterite at low stress. *Physics of the Earth and Planetary Interiors*, 19(3), 263-274.  
303 [https://doi.org/10.1016/0031-9201\(79\)90027-X](https://doi.org/10.1016/0031-9201(79)90027-X)
- 304 8. Duval, P., Ashby, M.F., & Anderman, I. (1983). Rate-controlling processes in the creep of  
305 polycrystalline ice. *Journal of Physical Chemistry*, 87(21), 4066-4074.  
306 <https://doi.org/10.1021/j100244a014>
- 307 9. Freed, A.M., Hirth, G., & Behn, M.D. (2012). Using short-term postseismic displacements to infer  
308 the ambient deformation conditions of the upper mantle. *Journal of Geophysical Research*,  
309 117(B1), B01409. <https://doi.org/10.1029/2011JB008562>
- 310 10. Gangi, A.F. (1983). Transient and steady-state deformation of synthetic rocksalt. *Tectonophysics*,  
311 91(1-2), 137-156. [https://doi.org/10.1016/0040-1951\(83\)90062-8](https://doi.org/10.1016/0040-1951(83)90062-8)
- 312 11. Hansen, L.N., Kumamoto, K.M., Thom, C.A., Wallis, D., Durham, W.B., Goldsby, D.L., et al.  
313 (2019). Low-temperature plasticity in olivine: Grain size, strain hardening, and the strength of the  
314 lithosphere. *Journal of Geophysical Research*, 124(6), 5427-5449.  
315 <https://doi.org/10.1029/2018JB016736>
- 316 12. Hansen, L.N., Wallis, D., Breithaupt, T., Thom, C.A., & Kempton, I. (2020). Dislocation creep of  
317 olivine: Low-temperature plasticity controls transient creep at high temperatures.  
318 <https://doi.org/10.1002/essoar.10504736.1>

- 319 13. Hanson, D.R., & Spetzler, H.A. (1994). Transient creep in natural and synthetic, iron-bearing  
320 olivine single crystals: Mechanical results and dislocation microstructures. *Tectonophysics*,  
321 235(4), 293-315. [https://doi.org/10.1016/0040-1951\(94\)90191-0](https://doi.org/10.1016/0040-1951(94)90191-0)
- 322 14. Hu, Y., Bürgmann, R., Uchida, N., Banerjee, P., & Freymueller, J.T. (2016). Stress-driven  
323 relaxation of heterogeneous upper mantle and time-dependent afterslip following the 2011 Tohoku  
324 earthquake. *Journal of Geophysical Research: Solid Earth*, 121(1), 385-411.  
325 <https://doi.org/10.1002/2015JB012508>
- 326 15. Kumamoto, K.M., Thom, C.A., Wallis, D., Hansen, L.N., Armstrong, D.E.J., Warren, J.M., et al.  
327 (2017). Size effects resolve discrepancies in 40 years of work on low-temperature plasticity in  
328 olivine. *Science Advances*, 3(9), e1701338. <https://doi.org/10.1126/sciadv.1701338>
- 329 16. Li, X., & Bhushan, B. (2002). A review of nanoindentation continuous stiffness measurement  
330 technique and its application. *Materials Characterization*, 48(1), 11-36.  
331 [https://doi.org/10.1016/S1044-5803\(02\)00192-4](https://doi.org/10.1016/S1044-5803(02)00192-4)
- 332 17. Li, Y., Bushby, A.J., & Dunstan, D.J. (2016). The Hall-Petch effect as a manifestation of the  
333 general size effect. *Proceedings of the Royal Society A*, 472.  
334 <https://doi.org/10.1098/rspa.2015.0890>
- 335 18. Masuti, S., Barbot, S., Karato, S.-I., Feng, L., & Banerjee, P. (2016). Upper-mantle water  
336 stratification inferred from observations of the 2012 Indian Ocean earthquake. *Nature*, 538, 373-  
337 377. <https://doi.org/10.1038/nature19783>
- 338 19. Moore, J.D.P., Yu, H., Tang, C-H., Wang, T., Barbot, S., Peng, D., et al. (2017). Imaging the  
339 distribution of transient viscosity after the 2016  $M_w$  7.1 Kumamoto earthquake. *Science*, 356(6334),  
340 163-167. <https://doi.org/10.1126/science.aal3422>
- 341 20. Muto, J., Moore, J.D.P., Barbot, S., Iinuma, T., Ohta, Y., & Iwamori, H. (2019). Coupled afterslip  
342 and transient mantle flow after the 2011 Tohoku earthquake. *Science Advances*, 5(9), eaaw1164.  
343 <https://doi.org/10.1126/sciadv.aaw1164>



- 344 21. Oliver, W.C., & Pharr, G.M. (2004). Measurement of hardness and elastic modulus by instrumented  
345 indentation: Advances in understanding and refinements to methodology. *Journal of Materials*  
346 *Research*, 19(1), 3-20. <https://doi.org/10.1557/jmr.2004.19.1.3>
- 347 22. Pharr, G.M., Herbert, E.G., & Gao, Y. (2010). The indentation size effect: A critical examination  
348 of experimental observations and mechanistic interpretations. *Annual Review of Materials*  
349 *Research*, 40, 271-292. <https://doi.org/10.1146/annurev-matsci-070909-104456>
- 350 23. Post, R.L. (1977). High-temperature creep of Mt. Burnet dunite. *Tectonophysics*, 42(2-4), 75-110.  
351 [https://doi.org/10.1016/0040-1951\(77\)90162-7](https://doi.org/10.1016/0040-1951(77)90162-7)
- 352 24. Qiu, Q., Moore, J.D.P., Barbot, S., Feng, L., & Hill, E.M. (2018). Transient rheology of the  
353 Sumatran mantle wedge revealed by a decade of great earthquakes. *Nature Communications*, 9,  
354 995. <https://doi.org/10.1038/s41467-018-03298-6>
- 355 25. Smith, B.K., & Carpenter, F.O. (1987). Transient creep in orthosilicates. *Physics of Earth and*  
356 *Planetary Interiors*, 49(3-4), 314-324. [https://doi.org/10.1016/0031-9201\(87\)90033-1](https://doi.org/10.1016/0031-9201(87)90033-1)
- 357 26. Syed Asif, S.A. & Pethica, J.B. (1997). Nanoindentation creep of single-crystal tungsten and  
358 gallium arsenide. *Philosophical Magazine A*, 76(6), 1105-1118.  
359 <https://doi.org/10.1080/01418619708214217>
- 360 27. Taylor, G.I. (1934). The mechanism of plastic deformation of crystals. Part I.- Theoretical.  
361 *Proceedings of the Royal Society A*, 145(855). <https://doi.org/10.1098/rspa.1934.0106>
- 362 28. Takeuchi, S., & Argon, A.S. (1976). Steady-state creep of single-phase crystalline matter at high  
363 temperature. *Journal of Materials Science*, 11, 1542-1566. <https://doi.org/10.1007/BF00540888>
- 364 29. Thom, C.A., Carpick, R.W., & Goldsby, D.L. (2018). Constraints on the physical mechanism of  
365 frictional aging from nanoindentation. *Geophysical Research Letters*, 45(24), 13,306-13,311.  
366 <https://doi.org/10.1029/2018GL080561>
- 367 30. Thom, C.A., & Goldsby, D.L. (2019). Nanoindentation studies of plasticity and dislocation creep  
368 in halite. *Geosciences*, 9(2), 79. <https://doi.org/10.3390/geosciences9020079>

- 369 31. Wallis, D., Hansen, L.N., Britton, T.B., & Wilkinson, A.J. (2017). Dislocation interactions in  
370 olivine revealed by HR-EBSD. *Journal of Geophysical Research: Solid Earth*, 122, 7659-7678.  
371 <https://doi.org/10.1002/2017JB014513>
- 372 32. Wallis, D., Hansen, L.N., Kumamoto, K.M., Thom, C.A., Plümper, O., Ohl, M., et al. (2020a).  
373 Dislocation interactions during low-temperature plasticity of olivine and their impact on the  
374 evolution of lithospheric strength. *Earth and Planetary Science Letters*, 543, 116349.  
375 <https://doi.org/10.1016/j.epsl.2020.116349>
- 376 33. Wallis, D., Hansen, L.N., Wilkinson, A.J., & Lebensohn, R.A. (2020b). Dislocation interactions  
377 in olivine control postseismic creep of the upper mantle. arXiv:2006.05195
- 378 34. Wang, L., Shum, C.K., Simons, F.J., Tapley, B., & Dai, C. (2012). Coseismic and postseismic  
379 deformation of the 2011 Tohoku-Oki earthquake constrained by GRACE gravimetry. *Geophysical*  
380 *Research Letters*, 39(7), L07301. <https://doi.org/10.1029/2012GL051104>